Polar-Direct-Drive Experiments at the National Ignition Facility

Introduction

In inertial confinement fusion (ICF), a capsule containing cryogenic deuterium–tritium (DT) fusion fuel is rapidly compressed to high temperatures and areal densities that are sufficient for thermonuclear fusion.[1–3] In laser-driven ICF, the compression drive is provided by coupling laser energy into an ablator surrounding a spherical fuel capsule, either directly via symmetric irradiation of the fusion target[4] or indirectly via a thermal x-ray bath generated from laser illumination of the inner walls of a cavity (hohlraum).[2] If the compressed central hot spot of an imploded capsule reaches a temperature of 5 keV or above and an areal density of at least 0.3 g/cm^2, the α particles generated via the D–T fusion reactions deposit their energy in the compressed core and the capsule can ignite.[5] Provided the confinement time determined by the inertia of the fuel mass is sufficiently long, the energy released via the fusion burn can exceed the incident driver energy and the energy gain exceeds unity. The demonstration of this concept is the primary mission of the National Ignition Facility (NIF),[6] a 192-beam laser delivering up to 1.8 MJ at a wavelength of 351 nm.

The current beam layout on the NIF is optimized for x-ray drive geometry where beams enter a cylindrical hohlraum through laser entrance holes along the polar axis, with no beams located around the equator. Figure 141.9(a) shows the NIF target chamber configured for x-ray drive with beam entry ports highlighted in blue. The optimum beam configuration for direct-drive target illumination is, however, spherically symmetric. The NIF target chamber was originally designed to support both the x-ray drive beam geometry and a symmetric beam layout by rearranging half of the beamlines to locations closer to the equator.[7,8] This is shown in Fig. 141.9(b) with the direct-drive ports highlighted in blue. Reconfiguring the NIF for a symmetric beam layout, however, poses a significant impact on NIF operations; therefore, the polar-direct-drive (PDD)[9] scheme was proposed to accommodate direct-drive experiments on the NIF using the indirect-drive beam configuration. Symmetric target irradiation is achieved by repointing beams increasingly toward the equator the farther they are located from the poles. This departure from
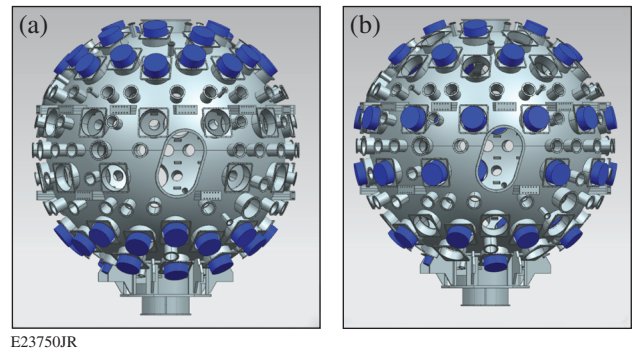

Figure 141.9
The National Ignition Facility (NIF) target chamber with beam ports highlighted. (a) The configuration for x-ray drive with beams clustered around the poles and (b) the symmetric configuration ideal for direct-drive inertial confinement fusion (ICF) experiments, with beams distributed uniformly around the chamber.

normal-incidence irradiation near the target equator leads to a drop in hydrodynamic efficiency and a reduction of kinetic energy imparted onto the shell.[10,11] To compensate for this effect, polar-direct-drive–ignition designs use increased drive energy toward the equator, beam profiles that include a skewed ellipse for the most-oblique beams, and DT ice layers of varying thickness (contoured shells) with lower mass around the equatorial region.[10,11]

This article presents results from PDD experiments on the NIF, designed to understand the effect of two-plasmon decay on preheat and cross-beam energy transfer on implosion energetics and symmetry.[11] This campaign is based on polar and symmetric direct-drive experiments on the OMEGA laser,[12] which provide a solid foundation for the PDD campaign on the NIF.[13,14] The experiments described here utilize the NIF in its indirect-drive configuration, including beam geometry, phase plates,[15] and beam smoothing by spectral dispersion (SSD).[16,17] Since the indirect-drive phase-plate spots are too small for direct-drive targets, they are operated out of best focus.[18] While this configuration is not suitable for full-scale, PDD-ignition experiments, it is highly valuable for initial studies of laser coupling, symmetry tuning, and laser–plasma

interactions. The goals of these early NIF experiments are (1) to develop a stable, room-temperature implosion platform to investigate laser deposition and laser–plasma instabilities at ignition-relevant plasma conditions and (2) to develop and validate ignition-relevant models of laser deposition and energy transport. Room-temperature, 2.2-mm-diam plastic shells were imploded with total drive energies ranging from approximately 500 to 750 kJ with peak powers of 120 to 180 TW and peak on-target intensities from 8×10^{14} to 1.2×10^{15} W/cm^2. Measurements of the shell-mass trajectory obtained via x-ray radiography agree reasonably well with 2-D *DRACO*[19] simulations when including the effect of cross-beam energy transfer (CBET)[20] in the calculations, while the ablation-surface trajectory inferred from self-emission images[21] is slower than simulations predict and increasingly deviates from the simulations at later times. Symmetry measurements are reproduced qualitatively by 2-D simulations, but it is expected that a 3-D treatment is required to fully capture the measured implosion shape. Modest hot-electron levels were inferred via hard x-ray emission[22] and are indicative of the two-plasmon–decay (TPD) instability.[23–25]

This article provides a description of laser–plasma interactions relevant to PDD and direct-drive ignition; presents the experimental setup and target parameters for the shots discussed herein; discusses shell trajectory and symmetry data obtained on PDD implosion experiments, followed by an examination of evidence for the TPD instability and the hot-electron population; presents future experimental plans and a brief overview of additional NIF capabilities required for a full-scale PDD ignition experiment; and summarizes our conclusions.

Laser–Plasma Interactions

Understanding and controlling the impact of parametric instabilities from intense laser–plasma interactions (LPI's) is a key requirement in ICF research. These can act as energy sinks and reduce the implosion velocity or give rise to hot electrons that can preheat the target and reduce target performance.[11] In the context of PDD, two instabilities are of particular importance: CBET[20] and the TPD instability.

In a direct-drive platform, CBET can arise when light rays in the wings of incident laser beams propagate past the target horizon and, on their outward trajectory, interact with incoming laser light. In an expanding plasma, this can result in energy transfer from the high-intensity region of the incoming beam to the low-intensity seed, thereby taking away energy from the capsule drive.[24] In polar-direct-drive geometry, this predominantly affects the equatorial region around $\theta = 90°$. This can be seen in Fig. 141.10, which shows calculated, instantaneous
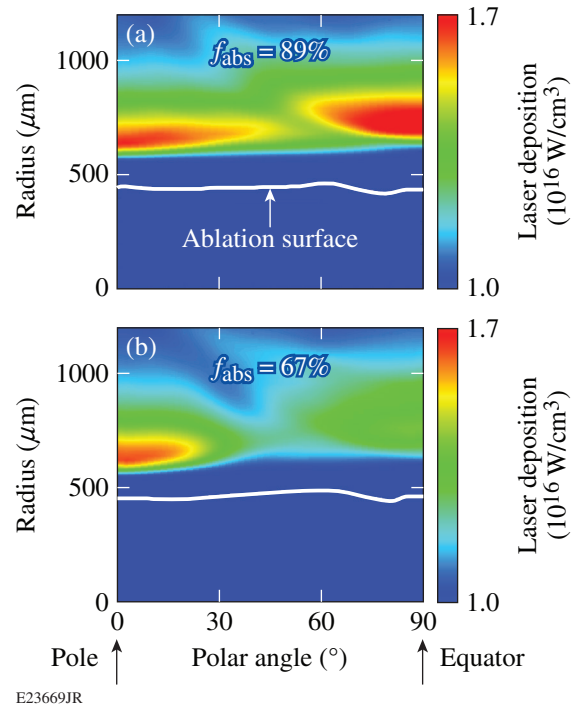

E23669JR

Figure 141.10

Calculated, instantaneous deposited laser power for polar-direct-drive (PDD) shot N130128 at 6.5 ns using the 2-D code *DRACO*: (a) collisional absorption only and (b) including cross-beam energy transfer (CBET). The integrated absorption in the presence of CBET is reduced by ~20%.

deposited laser power for a NIF PDD implosion experiment.[26] The simulations were performed using the 2-D hydrocode *DRACO*,[19] including a full 3-D laser ray trace,[27] a flux-limited heat-conduction model (with a flux limiter $f = 0.06$), and multi-group diffusive radiation transport with opacity tables from the Los Alamos astrophysical opacity library.[28] Figure 141.10(a) shows the calculated absorption without CBET, whereas Fig. 141.10(b) includes CBET. These calculations show a drop in deposited laser power near the equator ($\theta \sim 90°$) in the presence of CBET, with the instantaneous absorption fraction integrated over the entire deposition region dropping by more than 20% from $f_{abs} = 89\%$ to $f_{abs}^{CBET} = 67\%$.

Two-plasmon decay is an instability in which the electromagnetic (EM) wave of the incident laser light parametrically decays into two longitudinal electron plasma waves.[24] The requirement for matching wave number and frequency of the combined decay products and the incident EM wave along with the plasmon dispersion relation limits this process to regions close to the quarter-critical density $\left(n_c/4\right)$ in the coronal plasma.[24] Characteristic signatures of the TPD instability are the emission of scattered light at odd half-integer harmonics of

the incident laser frequency $(\omega_L/2$ and $3/2\omega_L)$ (Ref. 24) and a component of several tens of keV in the x-ray emission.[29,30] The hard x rays are a result of energetic electrons being accelerated in the presence of the TPD. Two-plasmon decay is relevant in direct-drive research because of its potential to result in anomalous absorption of laser light in the coronal region below the quarter-critical density and the acceleration of hot electrons to energies above 20 keV (Refs. 29 and 31). Hot electrons can penetrate the ignition target and prematurely heat the fuel, raising the fuel adiabat and resulting in lower compression and reduced target performance. The mechanism and magnitude of hot-electron production can change during the implosion, and the acceptable level of hot-electron preheat increases as the capsule is compressed and as the areal density and the electron stopping power of the imploded shell grow.

Experimental Setup

Figure 141.11(a) shows a typical target used for the first series of PDD experiments on the NIF. The targets were room-temperature, 2.2-mm-diam plastic shells with a wall thickness of 100 μm, typically filled with ~20 atm of D_2 gas. The target is placed at the NIF's target chamber center and irradiated with 192 laser beams. The 192 beams are divided into 48 groups of four beams (quads), arranged in four cones per hemisphere sharing the same polar angle at 23.5° and 30° (inners) and 44.5° and 50° (outers), respectively. The drive and implosion symmetry were tuned by repointing both quads and individual beams and also through separate pulse shapes defined for each cone of quads. The beam-pointing scheme is illustrated in Fig. 141.11(b), with circles denoting original quad-port locations, and the other symbols indicating repointed beam or quad positions on the initial target surface at $r = 1.1$ mm. The arrows show pointing shifts for each cone. The quads located in the 23.5° cone are not repointed and remain at their original orientation; all other quads are increasingly pointed toward the equator with decreasing latitude. The quads originating at 30° are shifted 5° toward the equator at the nominal target surface. Quads in the outer cones are split, and the beams in cones 3 and 4 are repointed in both polar and azimuthal angles. All four beams in 44.5° quads are pointed to individual locations, as indicated by the four arrows starting from a 44.5° quad location in Fig. 141.11(b). Beams in the 50° cone are used to illuminate the equatorial region of the target. These beams experience the largest repointing at ~33° toward the equator, with two beams per quad sharing the same focus point.
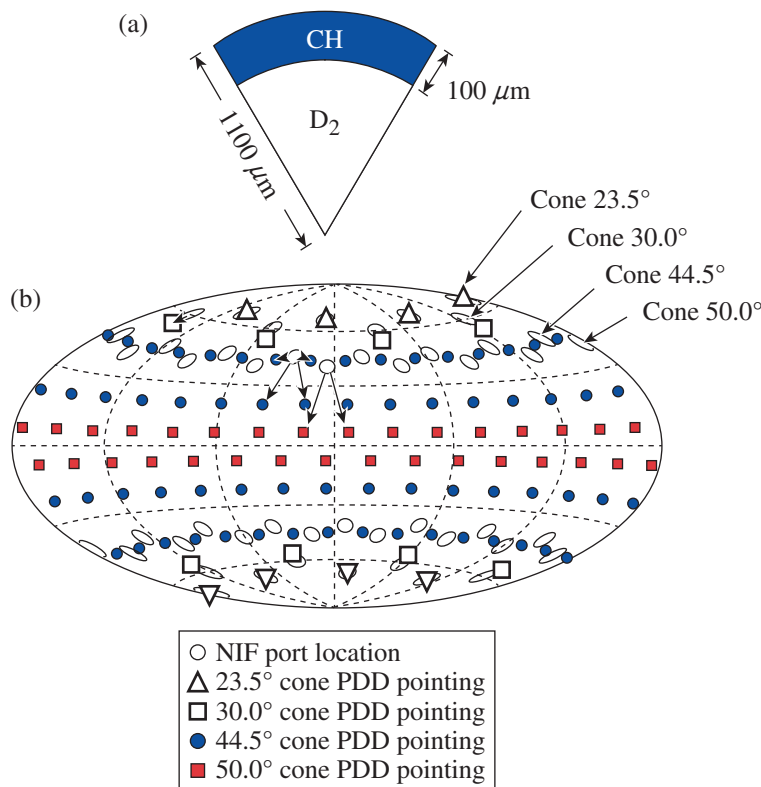

Figure 141.11
(a) Typical target used for the first series of PDD experiments on the NIF. (b) Beam pointing in PDD experiments, illustrated with respect to the initial target surface. Open circles denote original port locations.

E23751JR

Typical pulse shapes for each cone are shown in Fig. 141.12(a) (Ref. 11). The pulse comprises a flat foot, setting the shell to a low adiabat of $\alpha \sim 3$ (ratio of pressure to the Thomas–Fermi pressure at peak density), followed by a continuous rise to the main drive that lasts for ~3 ns. The pulse shapes between individual cones differ slightly for improved implosion symmetry. The total requested power for this shot (N131210) peaks at 124 TW and is shown in Fig. 141.12(b) as the dashed line. This corresponds to an overlapped intensity at the nominal target radius of $r = 1.1$ mm of 8×10^{14} W/cm^2. The total delivered laser power on this shot is shown as the solid line in Fig. 141.12(b), containing a total energy of 609 kJ. Figure 141.12(c) shows a hard-sphere projection of the normalized on-target intensity distribution at the nominal capsule radius of 1.1 mm. It can be seen that the intensity along the equator at $\theta \sim 90°$ is enhanced to offset the reduced hydroefficiency of the non-normal incidence beams driving the equatorial shell acceleration. The achievable target performance is limited since the experiments are performed with indirect-drive phase plates and beam smoothing. Direct-drive experiments require better beam smoothing than x-ray drive,[10] and the currently available NIF beam smoothing limits PDD experiments to modest laser intensities and low-convergence implosions to maintain shell integrity during the implosion. Furthermore, the achievable drive uniformity determined by the use of indirect-drive phase plates is expected to be limited even with an optimized pointing on the capsule (see also **Shell Trajectory and Symmetry**, p. 17).

The shell trajectory and symmetry were measured by imaging the imploding capsule from both the equatorial and polar directions using gated x-ray diagnostics (GXD's).[32,33] These record multiple x-ray images of the target evolution over the course of one experiment by using a high-voltage pulse (gate) that propagates the length of a stripline, i.e., the active region of the camera. Individual images are integrated over ~100 ps, as set by the gate width. The imaging system typically used a pinhole array with a pinhole diameter between 20 and 40 μm and beryllium filtration to reject optical and x-ray emission below ~1 keV. Spectrally and temporally resolved backscattered light between 450 and 750 nm is recorded using the full-aperture backscatter station (FABS).[34] The time-resolved hot-electron distribution is inferred by measuring the hard x-ray emission using the filter-fluorescer x-ray diagnostic (FFLEX).[22] FFLEX is an absolutely calibrated, time-resolved ten-channel spectrometer operating in the 20- to 500-keV range. Lastly, a suite of nuclear diagnostics measures the absolute neutron yield and temperature using neutron time-of-flight (nTOF) detectors,[35] the time of peak neutron emission using the particle time-of-flight (PTOF) diagnostic,[36] and the total areal densities using wedge-range-filter (WRF) proton spectrometers.[37]
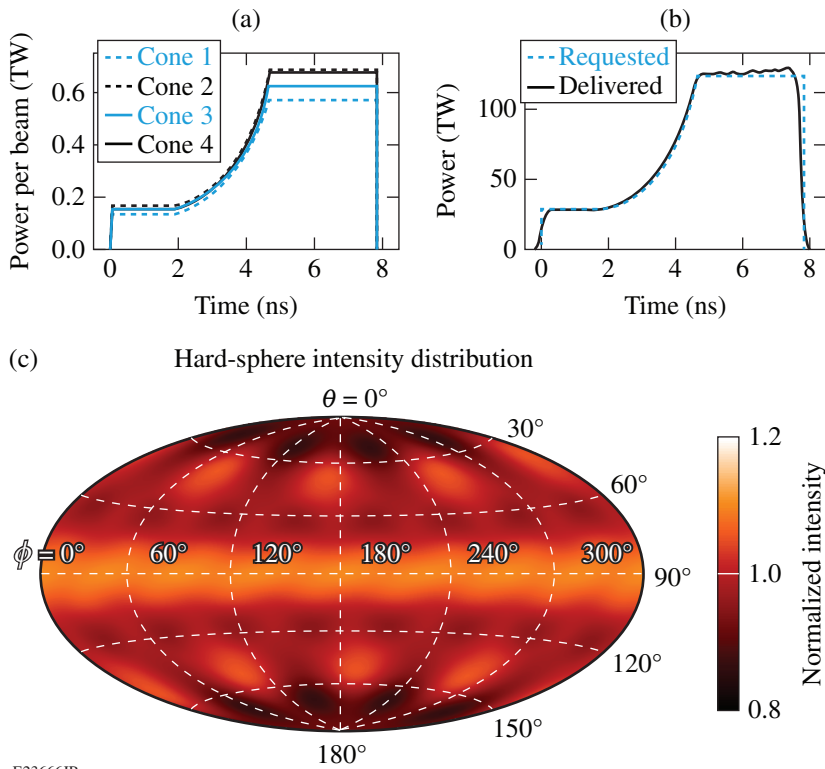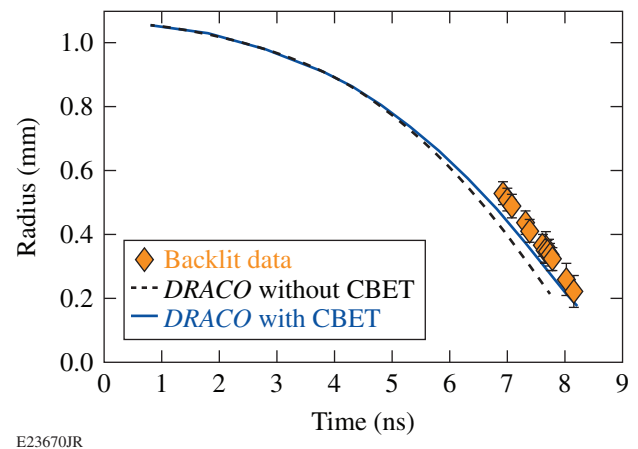

Figure 141.12
(a) Pulse shapes in each cone for shot N131210 comprising a low foot to set the shell adiabat followed by a slow rise to peak intensity. (b) Comparison between requested and delivered total pulse shapes. (c) Hard-sphere projection of the intensity distribution at the initial target radius. The intensity is increased near the equator to compensate for the reduced hydroefficiency of the energy deposited there.

E23666JR

Shell Trajectory and Symmetry

The shell trajectory is an important measure of how efficiently the incident laser energy is coupled to the imploding targets. Based on the work described in Ref. 38, an x-ray radiography platform using an areal backlighter was developed to image the shell position in an imploding capsule from the equatorial direction. In this technique, two of the NIF's 48 quads were redirected from the capsule to an iron backlighter foil located 5 mm from capsule center in the equatorial plane. The backlighter was irradiated with ~25 kJ using a 2-ns square pulse, generating Fe He$_\alpha$ emission at 6.7 keV over an ~1.5-mm-diam spot. Of the remaining 184 beams driving the capsule implosion, 16 beams were repointed and increased in energy by 50% to compensate for the missing drive from the backlighter beams. Radiography data were recorded with GXD's. Individual images of the framing-camera data were matched to the pinhole layout in the imaging setup, providing an accurate measurement of the image magnification and size. The gate velocity, i.e., the time between individual images, and interstrip delays were measured in offline calibrations, which, in conjunction with a measurement of the trigger time of the first strip on the camera, determined the timing of each recorded frame to within 50 ps. An example of a backlit image from shot N140612-001 at a radius of ~350 μm is shown in Fig. 141.13(a). In the image, the bright outer feature is the backlighter, with the central darker ring corresponding to the shell mass that has partially absorbed the backlighter emission. This made it possible to track the point of peak absorption as a function of polar angle, as highlighted by the white line in Fig. 141.13(a). Figures 141.13(b) and 141.13(c) are synthetic backlit images from 2-D *DRACO* simulations. The shape of the compressing shell is better modeled with the inclusion of CBET in the simulation [Fig. 141.13(c)] compared to the simulation without CBET [Fig. 141.13(b)]. This is discussed in detail later.

Performing the same analysis on multiple images over a single experiment provides a portion of the shell trajectory.

Figure 141.14 shows the extracted radius of an imploding shell, given by the peak absorption, as a function of time (diamonds). These data represent the accumulated trajectory data over two NIF shots (N140612-001 and N140816) with nominally identical experimental parameters such as target size and incident laser power, with high reproducibility of the experimental results. Temporal overlap in the measurements ensures that, within the measurement uncertainty, the same trajectory is observed for both shots. To generate synthetic radiography data, *DRACO* simulations of the implosion experiment are post-processed with the code *Spect3D*,[39] which transports x rays through the *DRACO* profiles, accounting for absorption using opacities generated by the PRISM group.[39] The detector resolution and the time window over which the images are integrated in the experiment are included in the post-processing. Examples of simulated radiography images are shown in Fig. 141.13 for a calculation without CBET [Fig. 141.13(b)] and with CBET [Fig. 141.13(c)]. In addition to the experimental data, Fig. 141.14

E23670JR

Figure 141.14

Two-dimensional *DRACO* simulations without CBET (dashed line) do not match the experimental shell trajectory extracted from radiography data (diamonds). By including CBET, the agreement improves (solid blue line).

N140612
$t = 7.75$ ns

DRACO
$t = 7.3$ ns

DRACO with CBET
$t = 7.5$ ns

1500 μm
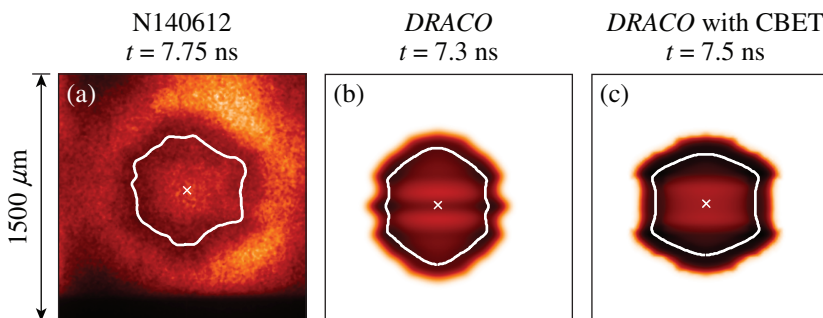
E23752JR

Figure 141.13

(a) Two-dimensional radiography data using 6.7-keV x rays to backlight the imploding PDD shell on shot N140612-001. The white line corresponds to the peak x-ray absorption. [(b),(c)] Synthetic radiography data from 2-D *DRACO* simulations without and with CBET, respectively.

also shows trajectory calculations with (solid blue line) and without CBET (dashed black line). Noticeably, the simulation result without CBET predicts an earlier capsule implosion, with the experimental trajectory data delayed by ~500 ps at the end of the observation window (~8 ns), and with the experimental trajectory converging by a factor of ~3 compared to ~5 in the simulation. When including CBET in the trajectory calculation, the discrepancy between experimental data and simulation reduces to ~200 ps. Between 7 and 8 ns, the shell exhibits a velocity of $v = 238 \pm 20$ km/s with an error of the shell radius of ~20 μm in the radiography data and ~50-ps timing uncertainty. The radial error is obtained by performing the trajectory analysis separately over each half of the radiography image. While the measured velocity agrees with the simulated value of 221 km/s of the CBET calculation over the same time interval (to within the error bars), the discrepancy in radial position of ~50 μm or 200 ps exceeds the uncertainty in the measurement. The delayed trajectory in the experiment compared to the calculation may indicate missing information in the simulations. A plausible hypothesis is that nonuniformities from laser imprint or initial shell-surface perturbations can grow via the Rayleigh–Taylor instability.[40,41]

A key requirement for an ICF platform is a high degree of spherical symmetry of the implosion to achieve maximum compression of the fuel and hot spot. Any deviations from spherical symmetry will result in transverse fuel motion and reduced conversion efficiency of the shell's kinetic energy into thermal hot-spot energy. In the case of PDD, the energy deposition is particularly compromised along the equator because of the indirect-drive beam geometry. Shell symmetry is extracted from the radiography data by fitting a superposition of low-mode Legendre polynomials from zeroth to tenth order

to the shape of the measured peak-of-emission lineout [white line in Fig. 141.13(a)]. In Fig. 141.15, the amplitudes of modes 2, 4, and 6 extracted from the backlit equatorial images of a single shot are plotted as a function of shell radius (diamonds). Amplitudes are displayed in units normalized to the shell radius (P_n/P_0). In this case, time is going from right to left as the capsule is compressed.

An alternative technique for extracting the modal evolution from radiography data is to image the soft x-ray self-emission of the coronal plasma at ~1 keV (Ref. 21). The combination of the limb effect and the optically thick shell results in a ring of soft x-ray emission in the image plane. The steep inner gradient of this image has been demonstrated to track with the ablation surface in directly driven implosions on OMEGA.[42,43] From these data, the shell symmetry is extracted from each frame by tracking the midpoint of the inner intensity gradient as a function of polar angle, followed by a Legendre-polynomial analysis as with the radiography data discussed above. Imaging the self-emission rather than backlighting the shell has the advantage of not requiring dedicated backlighter beams. The backlighter beams are not available for irradiation of the implosion target, which compromises the symmetry and hydrodynamic performance of the implosion. Additionally, the high signal-to-background ratio of the self-emission data results in an intrinsically lower uncertainty in extracting the inner-gradient midpoint for shape analysis compared to using the point of peak absorption in the radiography data. Because of its reliance on sufficient coronal plasma emission, self-emission imaging is limited to times during which the laser is incident onto the target since the coronal temperature quickly drops without laser illumination. This is in contrast to backlit imaging, which requires low self-emission. The opacity of the compressed shell in current
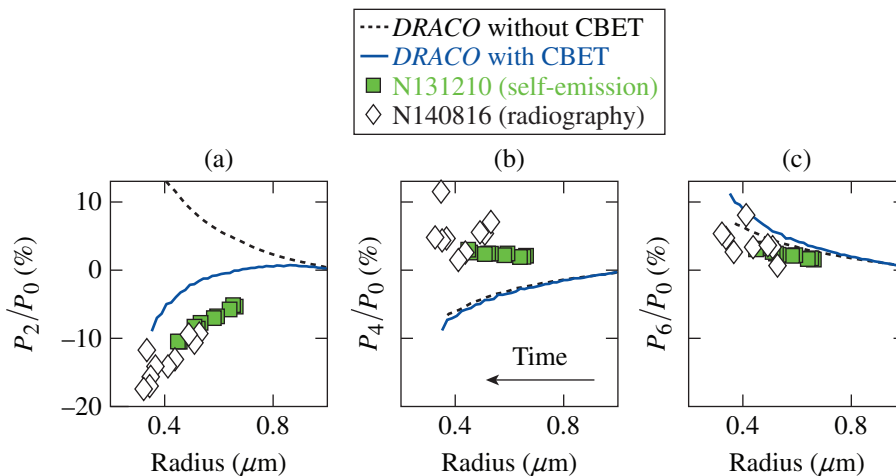

Figure 141.15
Equatorial shape evolution of an imploding PDD capsule. Modal amplitudes normalized to the shell radius are shown for (a) P_2, (b) P_4, and (c) P_6. Data are plotted as a function of shell radius, with time going from right to left. Diamonds are extracted from radiography data of shot N140816; squares are extracted from self-emission images on shot N131210. Lines show 2-D *DRACO* simulation results for shot N131210 with (solid) and without (dashed) CBET in the calculations.

E23674JR

PDD implosion experiments requires backlighter x rays in the range of 6 to 8 keV for optimal image contrast. At that photon energy, the coronal emission of a driven capsule is still bright enough to reduce the achievable signal-to-background ratio and to compromise a radiography measurement. Radiography imaging performs best in the absence of capsule drive, and radiography data were obtained with truncated laser pulses. The two techniques should be considered complementary since they can probe different times in a given implosion.

Two examples of self-emission data are displayed in Fig. 141.16. These data were acquired on the same shot and at roughly the same time at a convergence ratio of CR ~ 2.5, with Fig. 141.16(a) being taken from the polar direction, looking down onto the target, and Fig. 141.16(b) from the equatorial direction at $\theta = 90°$ using port (90,78). The elongated feature visible on the left in Fig. 141.16(a) is the stalk holding the target, which is located behind the capsule in Fig. 141.16(b) and is not visible in the equatorial data. In the case of the equatorial image, the implosion shape exhibits visible low-mode asymmetry, with, e.g., a noticeable P_6 mode of $P_6/P_0 \approx 2.5\%$. In contrast, the polar image is far more symmetric and the Legendre analysis gives $P_6/P_0 \approx 0.2\%$. This difference in asymmetry is a result of the NIF beam geometry for x-ray drive; it impacts the target illumination as seen from the equator. This is compounded by the use of indirect-drive phase plates that are not optimized for PDD illumination. The polar image is significantly more symmetric because the beams are arranged azimuthally symmetric around the target.
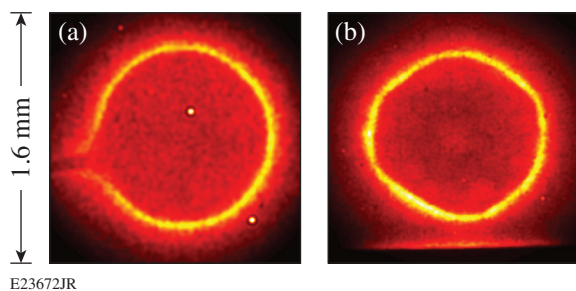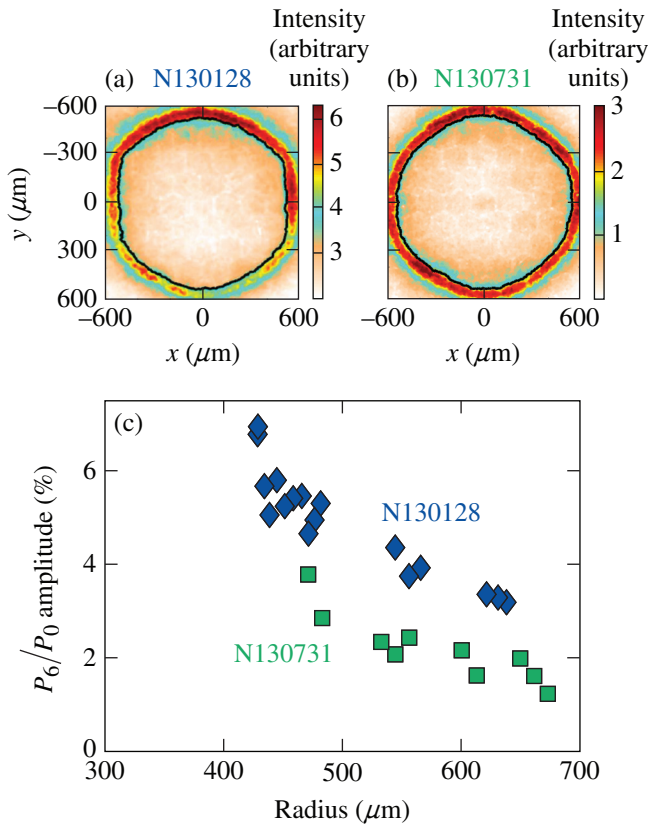

Figure 141.16
Self-emission images of an imploding PDD capsule on shot N131210 as seen from (a) the polar direction at 7.0 ns and (b) the equator at 7.3 ns.

Symmetry data extracted from equatorial self-emission images such as Fig. 141.16(b) are shown in Fig. 141.15 as the square data points. It should be noted that these data were not acquired on the same shot as the radiography images (diamonds). For both experiments, the target parameters such as target size, shell thickness, and gas fill, as well as the incident laser power

and beam pointing, were nearly identical. The two measurement techniques—radiography and self-emission imaging—probe different surfaces of the target, which do not necessarily exhibit the same low-mode asymmetry. Since the shell is relatively thin compared to the wavelengths of the modes plotted in Fig. 141.15, it is not surprising that the data generally show comparable modal amplitudes with excellent reproducibility between shots. The self-emission data show considerably less scatter because of the intrinsically higher resolution of the well-defined inner-gradient feature in the self-emission images. This validates using self-emission imaging as a tool for tracking low-mode asymmetries in PDD implosion experiments.

Also shown in Fig. 141.15 are results of the simulated mode evolution from 2-D *DRACO* simulations for shot N131210 [self-emission data (squares)]. Similar to the trajectory data in Fig. 141.14, calculations with (blue solid line) and without (black dashed line) CBET are shown. The biggest difference is observed for the P_2 mode, which evolves in the no-CBET case with a positive P_2 amplitude (prolate) with the equator slightly overdriven with respect to the pole. In contrast, the CBET calculation predicts a negative P_2 (oblate) with an underdriven equatorial region [see also Figs. 141.13(b) and 141.13(c)]. For modes P_4 and P_6, the differences between the two simulations are small, further underlining the importance of CBET on the equatorial energy deposition in PDD geometry. The negative P_2 observed in the CBET calculation qualitatively matches the experimentally observed P_2 evolution, although the calculation underpredicts the P_2 amplitude by ~50%. The same trend is seen for the P_6 evolution, although the no-CBET calculation is slightly closer to the experiment than the CBET calculation. The biggest discrepancy between simulations and experiment is observed for the P_4 amplitudes, with simulations predicting a distinctly negative P_4, whereas the experimental data exhibit a marginally positive P_4 at a few percent. This discrepancy may be caused by 3-D effects that are not modeled with 2-D *DRACO*. The intensity distribution on the target is inherently three dimensional, and a 2-D calculation is not expected to fully capture these details. Three-dimensional simulations with the hydrodynamic code *HYDRA*[44] are being planned to investigate these effects.

A primary goal of the early NIF PDD experiments was to demonstrate tunability of the implosion symmetry. Figures 141.17(a) and 141.17(b) show equatorial self-emission images from two separate shots, both recorded at a CR ~ 2. The first shot [Fig. 141.17(a)] exhibited a pronounced P_6, and a subsequent shot [Fig. 141.17(b)] was tuned specifically to reduce the P_6 amplitude by adjusting the beam pointing and

TC10695hJR

Figure 141.17
Demonstration that improved symmetry can be obtained by tuning beam pointing and the power balance between NIF cones. [(a),(b)] Equatorial self-emission images of shots N130128 (before retuning) and N130731 (after retuning), both at a convergence ratio (CR) ~ 2. (c) P_6 amplitude normalized to the shell radius as a function of the shell radius, with time going from right to left. Shot N130128 [(a) and diamonds in (c)] exhibits a pronounced P_6 amplitude, which was reduced by ~50% in N130731 [(b) and squares in (c)].

power balance. The respective P_6/P_0 evolution is shown in Fig. 141.17(c). The P_6 amplitude was reduced by ~50% between the two experiments, consistent with amplitudes observed in subsequent implosions [see, e.g., Fig. 141.15(c)], but is still non-negligible. Given the currently available NIF hardware optimized for x-ray drive platforms, there are limitations to the level of achievable symmetry. To improve on the uniformity achievable with the current indirect-drive phase plates, PDD phase plates are currently in production to optimize the irradiation profile and generate more-symmetric implosions.[10] The phase plates will correct the reduced hydroefficiency near the equator with a focal-spot profile containing a secondary ellipse. First experiments with these phase plates are anticipated in 2017. It should be noted that the currently available phase plates and achievable symmetry are adequate for the initial primary goals of the PDD campaign, i.e., to study laser coupling, symmetry tunability, and LPI's under NIF-relevant conditions.

The primary purpose of the self-emission imaging is to extract symmetry information, but it is also possible to track the implosion trajectory via the ablation surface. Figure 141.18 shows trajectory data extracted from self-emission images (squares) obtained on shot N140612-001, one of the two shots for which the radiography data are shown in Fig. 141.14. Figure 141.18 also shows 2-D *DRACO* simulations of the ablation-surface trajectory (solid line). In this case, only the calculation including CBET is shown. As with the x-ray radiography, simulated self-emission images were generated by post-processing *DRACO* simulations with *Spect3D*.[39] It can be seen that, as the implosion progresses, the self-emission data increasingly lag the simulation results, with a delay of nearly 700 ps for the latest measurements at ~7 ns. This is in contrast to the trajectory extracted from radiography data (Fig. 141.14), which agrees reasonably well with the simulations. This effect may be partially explained by nonuniformity growth on the ablation surface or preheat from the corona, both of which can result in decoupling the ablation surface from the shell. The outer-surface root-mean-square (rms) roughness of these targets is nearly a factor of 4 higher than the NIF standard (55-nm rms between modes 51 to 1000 compared to 14-nm rms). In addition, the indirect-drive beam smoothing is lower than that required for high-convergence direct-drive implosions,[10] and instability growth from laser-seeded imprint may be significant in these experiments.

This expectation is corroborated by measurements of the areal density (ρR), which typically range from 120 to 150 mg/cm^2, while simulations predict 120 to 280 mg/cm^2, depending on the time of measurement. The areal density is measured at the time of peak fusion yield via the downshifted proton spectrum,[37] and
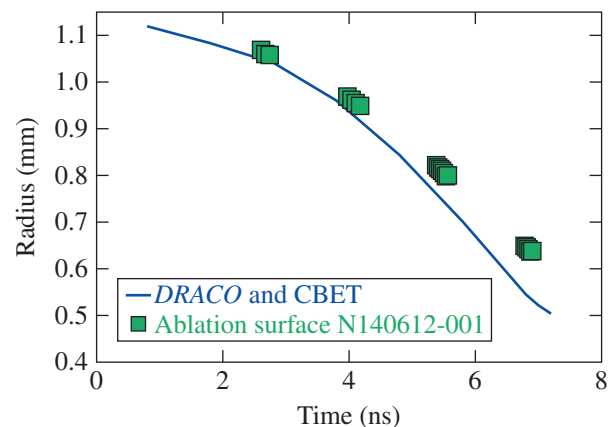
E23675JR

Figure 141.18
Comparison of trajectory data extracted from self-emission images (squares) and 2-D *DRACO* simulations with CBET (solid line).

it is possible that this is not equivalent to the time of peak ρR in the simulations. Uncertainties in the shell trajectory and the time of peak emission result in a range of possible values for areal density from the simulations. For example, instability growth on the inside of the ablator may penetrate into the hot spot and quench the fusion reactions early compared with simulations, as has been observed in OMEGA implosions.[45] Future experiments will investigate Rayleigh–Taylor growth from laser imprint and shell nonuniformities in PDD geometry.[46] Improved beam smoothing is a required capability for full-scale, PDD-ignition experiments (see also **Future Experiments and Additional NIF Capabilities**, p. 24). In conclusion, while the agreement between simulation results and the measured shell trajectory (as given by the radiography data) provides some confidence in the modeling of laser-energy coupling to shell kinetic energy, the mismatch with the self-emission data and the role of nonuniformity growth must be better understood.

Two-Plasmon Decay in Polar Direct Drive

Both planar[31,47] and spherical implosion experiments[48,49] on the OMEGA Laser System[12] have demonstrated the production of a hot tail on the electron distribution function that has been associated with the TPD instability.[48] This association has been determined on the basis of the temporal coincidence between half- and three-halves-harmonic emission and hard x-ray production.[48] For long-scale-length ($\sim$350-μm) targets irradiated at the highest overlapped (vacuum) laser intensities ($\sim$7 $\times$ 10^{14} W/cm^2), this tail was shown to exhibit a slope temperature of 60 to 80 keV (Refs. 47 and 50) and contain a few percent of the total incident laser energy.

In direct-drive experiments, TPD is a multibeam instability that requires several laser beams to cooperate (by sharing decay waves) in order to overcome the instability threshold[51] that is assumed to arise primarily because of density inhomogeneity (characterized by the scale length L_n). Expressions for the threshold of multibeam TPD were obtained by *ad hoc* use of the Simon *et al.* threshold,[48,52] by computing the maximum convective gain for common waves,[53] or by numerical solution of the TPD equations in three dimensions.[54] In all cases the threshold for the onset of the TPD instability is seen to depend on the quantity $I_L L_n / T_e$, where I_L is the overlapped intensity *resulting from a subset of the incident beams* (determined by a symmetry condition), L_n is the density scale length, and T_e is the electron temperature. Additional factors modifying the threshold arise as a result of beam polarization and beam-incidence angles.[55] A simple extrapolation of OMEGA/OMEGA EP data to the NIF (i.e., by computing $I_L L_n / T_e$ with the total overlapped intensity) would suggest that similar, or greater,

levels of hot electrons are to be expected in PDD-ignition targets, mainly because of the larger scale length but partially mitigated by higher coronal temperatures. These levels would lead to an unacceptable amount of preheat. However, significant differences exist between experiments on OMEGA and the NIF that may result in different TPD behavior—these motivate, in part, the present experiments. In NIF PDD experiments many more beams are overlapped. The beam symmetry and incidence angles also differ, leading to uncertainties in which beams are to be included when computing the overlapped intensity. It is speculated that because of the characteristics of the beam overlap on the target, the TPD instability will be able to share decay waves most effectively along the polar axis and around the equatorial region.

The TPD instability can be identified via the energetic electrons and hard x rays that it produces. Hard x-ray spectra are measured in NIF PDD experiments with the FFLEX diagnostic,[22] measuring the temporal history of the bremsstrahlung spectrum in the 20- to 500-keV range using ten individually filtered, time-resolved detectors. It provides the basis for extracting the characteristics of the hard x-ray spectrum and consequently the energetic electron distribution.[56,57] FFLEX integrates the x-ray emission over a field of view of ~100 mm at target chamber center without spatial resolution.

A typical hot-electron spectrum produced in a NIF PDD experiment (shot N131210) is shown in Fig. 141.19. For this shot, a total laser energy of E_L = 609 kJ was incident on the target, corresponding to a nominal overlapped intensity at the target surface (r = 1.1 mm) of 8 $\times$ 10^{14} W/cm^2. *DRACO*
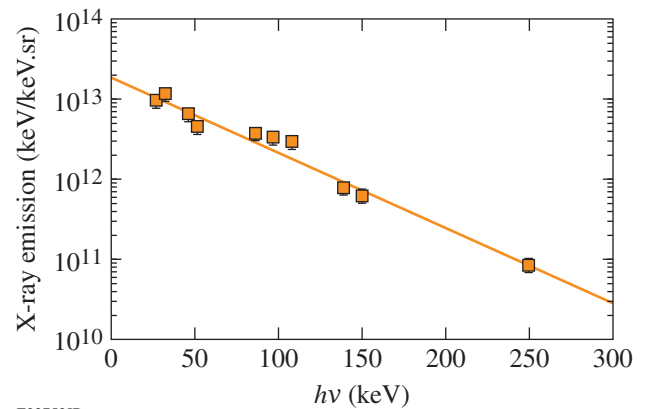
E23753JR

Figure 141.19
Time-integrated FFLEX analysis for shot N131210. The squares denote total emission as measured by the FFLEX detector; the solid line is the fitted x-ray spectrum giving a hot-electron component in the experiment at a temperature of 46±2 keV and with a total energy content of 2.5±0.3 kJ.

simulations (including CBET) suggest that, at the time of strong hot-electron production ($t = 6$ ns), the peak intensity (polar angle averaged) at the quarter-critical density surface was $\sim 3.5 \times 10^{14}$ W/cm^2, with a density scale length of ~ 360 μm and a coronal temperature of ~ 3.2 keV (Table 141.I). For later times ($t = 7$ ns) the quarter-critical intensity, density scale length, and electron temperature increase slightly (by $\sim 10\%$, $\sim 5\%$, and 10%, respectively). In Fig. 141.19 the squares show the measured, time-integrated x-ray emission for the ten FFLEX channels, and the solid line represents the one-temperature, x-ray emission fit through the data. The standard fit to the FFLEX data yields a time-averaged temperature of $T_e \sim 46\pm2$ keV, with a total energy content in the hot electrons of $E_{hot} \sim 2.5\pm0.3$ kJ. This temperature is consistent with recent experiments on the OMEGA Laser System,[49] where TPD is known with some certainty to be the origin. For this analysis it was assumed that hot electrons deposit their energy in the plastic ablator, with negligible attenuation of the x-ray emission in the shell material or the coronal plasma. In contrast to typical two-temperature distributions for indirect-drive ICF platforms,[58] NIF PDD experiments are typically well fit by a one-temperature distribution.

The hot electrons observed here are attributed to TPD rather than stimulated Raman scattering (SRS). SRS hot electrons are typically expected to be of somewhat lower temperatures (i.e., as observed by Döppner et al.[58] in indirect-drive experiments). The scattered-light spectrum (Fig. 141.20) collected in the FABS diagnostic located in beam 315, quad Q31B, indicates that SRS is excited, but the low measured SRS reflectivity <0.1% is not consistent with a 0.4% energetic electron fraction (as deduced from FFLEX data). This conclusion does not take into account illumination nonuniformities that may drive SRS in places not observable by the FABS (i.e., at the target equator, beam 315 irradiates the mid-latitudes of the southern
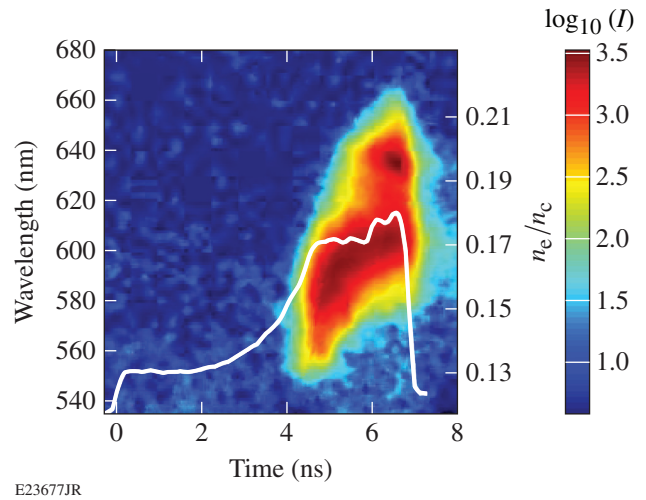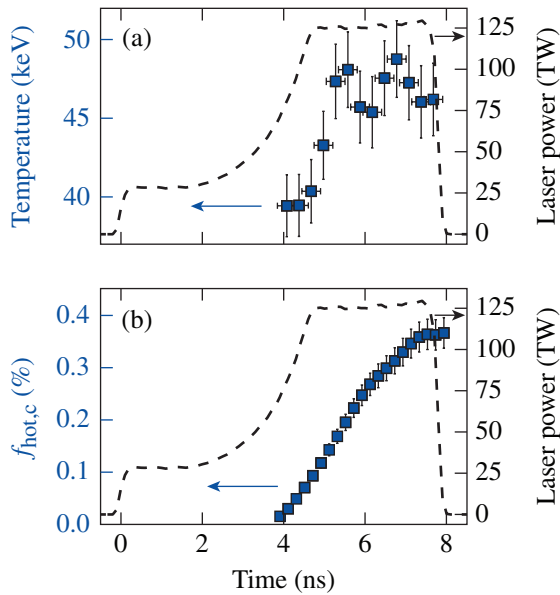

Figure 141.20
Stimulated Raman scattering spectrum obtained on shot N140816 using the full-aperture backscatter station (FABS) in quad Q31B at a polar angle of $\theta = 152°$. The white line is the incident laser power in the experiment.

hemisphere of the target at a polar angle of $\theta \sim 152°$). Figure 141.20 shows that the SRS spectrum increases in time from wavelengths of 550 nm to 650 nm, corresponding to a shift in the maximum electron density of the SRS active region from 0.13 n_c to 0.22 n_c, where n_c is the critical density. It is speculated that the SRS region moves to higher densities with time because of the $I_L L_n / T_e$ dependence of the SRS convective gain.

A time-resolved FFLEX analysis of the same shot (N131210) is shown in Figs. 141.21(a) and 141.21(b). In both plots the squares are experimental data and the dashed lines denote the incident total laser power in the experiment as a temporal reference. The temperature history [Fig. 141.21(a)] shows $T_e \sim 47$ keV during the peak intensity portion of the incident laser pulse, with no hard x-ray emission observed during the foot up to ~ 4 ns. The time-resolved, total cumulative conver-

Table 141.I: Representative parameters for the PDD experiments shown in Fig. 141.22. The laser intensity, density scale length L_n, and electron temperature T_e are evaluated from *DRACO* calculations (averaged over polar angle θ), including CBET (except where noted), at the quarter-critical density surface for $t = 6$ ns. The threshold parameter η is described in the text.

Ablator material	Nominal laser intensity (W/cm^2)	Energy on target E_L (kJ)	I_L (W/cm^2)	L_n (μm)	T_e (keV)	η
CH	8×10^{14}	490 to 660	3.5×10^{14} 5.5×10^{14} (no CBET)	360	3.2	1.7
CH	1.2×10^{15}	645	4.6×10^{14} 6.1×10^{14} (no CBET)	360	3.5	2.0
CH + Si	1.2×10^{15}	760	4.6×10^{14} 6.7×10^{14} (no CBET)	310	4.5	1.4

E23678JR

Figure 141.21

Time-resolved FFLEX analysis for shot N131210 (compare Fig. 141.20). The dashed line is the total incident laser power. (a) The hot-electron temperature and (b) the time-resolved, total conversion efficiency of incident laser energy into hot electrons. At the end of the laser pulse, ~0.4% of the incident energy has been converted into energetic electrons.

sion efficiency of incident laser energy into hot electrons $f_{\text{hot,c}}(t)$ [Fig. 141.21(b)] is a guide to target preheat. This efficiency is defined by

$$f_{\text{hot,c}}(t) = \int_0^t E_{\text{hot}}(t')\mathrm{d}t' \bigg/ \int_0^t E_{\text{L}}(t')\mathrm{d}t',$$

where $E_{\text{hot}}(t)$ and $E_{\text{L}}(t)$ are the instantaneous energy converted into hot electrons and the incident laser energy, at time t, respectively. The sharp rise, starting at $t \sim 4$ ns, is followed

by a roll-over and saturation near the end of the laser pulse, leading to a total conversion efficiency of $f_{\text{hot}} \sim 0.4\%$.

The total hot-electron fraction $f_{\text{hot}} = E_{\text{hot}}/E_{\text{L}}$ is shown in Fig. 141.22 for six PDD shots. Data obtained at nominal overlapped intensities of $\sim 8 \times 10^{14}$ W/cm^2 with various pulse durations (6.8 to 8.5 ns, E_{L} = 490 to 660 kJ) are marked as the open circles. These data exhibit hot-electron fractions of $f_{\text{hot}} \sim 0.4\%$ characterized by a temperature of $T_{\text{e}} \sim 50$ keV.

It is estimated that if more than ~0.15% of the laser energy is coupled into a direct-drive–ignition target in the form of hot electrons, the target performance will be negatively affected.[59] To compute the preheat resulting from a given hot-electron source, several factors must be taken into account.[49] Based on the results of Yaakobi et al.,[49] it is estimated that ~25% of the hot electrons produced will intersect the target and result in preheat. This leads to an estimated upper limit of ~0.6% for the tolerable hot-electron production in PDD-ignition experiments. The observed hot-electron generation in current NIF PDD experiments with nominal intensities of 8×10^{14} W/cm^2 falls below this limit and is therefore a promising result. Nonetheless, the current experiments are not full scale, and CBET is expected to have lowered the intensity at $n_{\text{c}}/4$ (Table 141.I). It is therefore essential that mitigation schemes be investigated and experiments be performed at a higher laser intensity and longer scale length (at the $n_{\text{c}}/4$ surface).

It has been observed in experiments on OMEGA,[47,60] and discussed in Refs. 48 and 61, that higher-Z coronal plasmas lead to a reduction in TPD hot electrons and increase the threshold intensity for its onset. The addition of an outer 13.5-μm Si layer to the plastic ablator has been investigated as a possible miti-
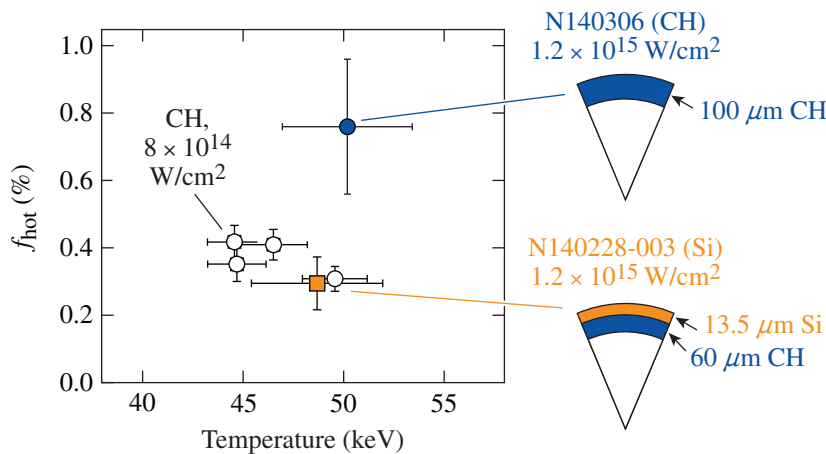
E23679JR

Figure 141.22

Hot-electron fraction from six PDD targets, mostly CH, irradiated with nominal peak intensity of 8×10^{14} W/cm^2 (open circles). Two shots were taken at 1.2×10^{15} W/cm^2; one with a CH ablator (solid circle), the other with a Si ablator (solid square).

gation strategy on NIF shot N140228-003. This is compared in Fig. 141.22 with a standard CH target (shot N140306), both of which were driven with a higher peak laser power of ~180 TW, corresponding to a nominal overlapped peak intensity of 1.2×10^{15} W/cm^2. The same foot intensity of ~30 TW was used as for the experiments with a nominal intensity of 8×10^{14} W/cm^2. The pulse driving the Si-layer target implosion was slightly longer by 0.5 ns, corresponding to a total incident energy of 760 kJ, compared to 645 kJ incident onto the pure-CH ablator target (Table 141.I). The hot-electron data for these two experiments are displayed as the blue solid circle (CH ablator) and the orange solid square (Si ablator) in Fig. 141.22. The hot-electron fraction for the $I_L = 1.2 \times 10^{15}$ W/cm^2, plastic-ablator experiment approximately doubled to $f_{hot} \sim 0.8\%$, while the Si-ablator experiment saw a reduction in the hot-electron fraction to $f_{hot} \sim 0.3\%$ (both relative to the 8×10^{14} W/cm^2 CH experiments). Since FFLEX does not identify the origin of the x rays, an assumption must be made about the material in which hot electrons lose their energy via bremsstrahlung emission. For the analysis of the Si-layer capsule displayed in Fig. 141.22, it was assumed that the Si was fully ablated and the electrons deposited their energy solely in the unablated plastic shell, with no attenuation of the x-ray emission by the coronal plasma. Since the thick-target bremsstrahlung equation (relating x-ray emission to hot-electron population) scales linearly with the effective Z of the target material, assuming electrons deposit their energy in both CH and Si, would necessarily further reduce the inferred energy in the hot-electron population. The analysis of the Si-ablator shot displayed in Fig. 141.22 is therefore a pessimistic interpretation. The actual hot-electron fraction may be lower and the mitigating effect greater than indicated in Fig. 141.22.

The lower observed hot-electron fraction in the Si-ablator target is consistent with an increased TPD threshold based on the simple $I_L L_n / T_e$ scaling. In previous OMEGA experiments TPD signatures were observed when the parameter $\eta = I_L L_n / 233 T_e$ exceeded unity. In this expression, I_L is in units of 10^{14} W/cm^2, L_n is in μm, and T_e is in keV. This empirical scaling is based on the Simon threshold for the absolute instability of a single plane wave.[52] It was generalized by Seka et al.[48] in an ad hoc way by substituting the total overlapped laser intensity at the $n_c/4$ surface in place of the single-plane wave intensity assumed by the theory. When this was done, the onset of TPD was well modeled over a range of different experiments on OMEGA. Table 141. I shows that, for the $I_L = 8 \times 10^{14}$ W/cm^2 reference case, $\eta = 1.7$ and TPD is expected (and observed) to be above threshold. The increase in hot electrons for the high-intensity CH ablator is consistent

with the larger value of $\eta = 2.0$. This increase in η is a result of a combination of larger scale length and higher laser intensity. In contrast, the Si-ablator experiment is predicted to have a reduced scale length, and a significantly higher electron temperature. As a result, the η parameter is lower ($\eta = 1.4$) than the reference experiment (marginally above threshold) and the hot-electron fraction behaves accordingly. The total overlapped intensity has been used here in the expression for the threshold parameter η. No account is made for beam symmetry requirements that are known to play a role in multibeam TPD.[54,62] These requirements would lead to a lower effective overlapped intensity.

Higher-Z ablator materials have disadvantages, such as a lower hydrodynamic efficiency, reduced heat conduction, and potential radiation preheat of the target core. Pure-Si ablators are, therefore, not an attractive solution for TPD mitigation. Therefore, current PDD-ignition target designs utilize multiple layers for an optimized coronal plasma[63] that include a thin mid-Z layer (e.g., Si) for LPI mitigation inside lower-Z material with better hydrodynamic performance.

Future Experiments and Additional NIF Capabilities

The PDD campaign on the NIF has started to investigate direct drive in integrated implosion experiments. It is clear that a detailed understanding of the physics governing implosion performance at NIF conditions and ignition scales will require dedicated platforms to decouple individual aspects of the implosion. In particular, hydrodynamic instability growth has been identified as an important factor in understanding the discrepancy between the simulated and measured shell trajectories (see **Shell Trajectory and Symmetry**, p. 17). Future experiments will investigate Rayleigh–Taylor growth[41] from shell surface perturbations and laser imprint in a spherical-implosion PDD platform on the NIF using cone-in-shell targets. Similar experiments have been used successfully to measure Rayleigh–Taylor growth in spherical convergent geometry for indirect drive on the NIF[64] and direct drive on OMEGA.[65]

It has been suggested that CBET is responsible for a significant reduction in absorption efficiency of the incident laser power, particularly near the equator (see **Shell Trajectory and Symmetry**, p. 17), and mitigating CBET is of key importance for developing a robust PDD-ignition platform for the NIF. A viable mitigation strategy for CBET is to introduce a wavelength separation between interacting beams.[63,66] To mitigate CBET in PDD experiments on the NIF, a hemispheric laser wavelength separation in excess of ±5 Å at $\lambda = 351$ nm has been proposed,[67,68] such that beams incident on the equa-

tor from the upper and lower hemispheres are separated in wavelength by >10 Å. This is expected to reduce the volume over which efficient CBET gain can occur at the equator and to recover a significant fraction of the CBET-incurred losses. The current NIF front end supports tunable wavelengths of up to approximately ±2.5 Å for each of the inner beam cones at 23.5° and 30° and for both outer cones combined (44.5° and 50°). This is insufficient for optimized CBET mitigation in NIF PDD implosions but is expected to be adequate to test this mitigation scheme. Using the nominal PDD pointing, only the outer-cone beams are incident near the equator of the target and wavelength separation at the equator is currently not supported. However, to test this CBET mitigation scheme, a hemispheric $\Delta\lambda$ shift can be achieved by repointing beams in one hemisphere such that inner-cone beams drive the equator from one hemisphere and overlap with outer-cone beams from the opposite side. With different wavelengths for inner and outer cones, this results in a nonzero, equatorial wavelength separation. The currently achievable wavelength detuning of ±2.5 Å between inner and outer cones is anticipated to increase the absorption fraction by ~5%, corresponding to ~25% of the total CBET-incurred losses.

It is important to understand hot-electron generation in NIF PDD implosions, and it is expected that successful CBET mitigation will result in an increase of the effective laser intensity at quarter-critical density and therefore an increase in the TPD gain, as discussed in **Two-Plasmon Decay in Polar Direct Drive** (p. 21). The TPD instability is believed to be strongest along the polar axis and around the equator, but it is difficult to decouple the contributions of these two locations in integrated implosion experiments. Future experiments will use planar targets to approximate the laser–target interactions and coronal conditions at the pole and the equator of a PDD target. This will be used to investigate the effect of the beam angle of incidence on the TPD instability and hot-electron production at NIF-relevant scale lengths and temperatures. Importantly, since planar targets exhibit a very high absorption efficiency, CBET seeded by backscattered light is not expected to be a significant source of laser-energy losses in these experiments.

In addition to a hemispheric wavelength separation capability with $\Delta\lambda > 5$ Å for CBET mitigation, additional NIF capabilities and hardware are required to support ignition-scale, cryogenic PDD experiments on the NIF. These are being implemented by the NIF PDD Laser Path Forward working group. The achievable uniformity in current direct-drive experiments is limited by the use of defocused indirect-drive phase plates; dedicated PDD phase plates are required for high-convergence

implosions. These are in production and first experiments with these phase plates are anticipated for 2017.

High beam-smoothing rates are required to limit the imprint of laser nonuniformities that can disrupt the implosion. Some instability mitigation is provided by the SSD system currently installed on the NIF,[16,17] but this is less than that required for PDD-ignition experiments.[10] One-dimensional SSD with multiple phase-modulation frequencies (multi-FM 1-D SSD)[69] has been developed at LLE to provide the smoothing level required for the current NIF polar-direct-drive–ignition point design. It is compatible with the existing NIF Laser System, and modifications required to implement multi-FM 1-D SSD on the NIF are limited to fiber-based systems in the Master Oscillator Room, in addition to a new diffraction grating in the preamplifier module.[10]

Polarization smoothing overlaps beams or beamlets of orthogonal polarization, to suppress interference between speckle patterns from different beamlets.[70] This provides instantaneous smoothing in addition to the SSD system.[71] The polarization smoothing currently used on the NIF employs a polarization rotation of two beams per quad to smooth out interference modulations between beams within a quad. This provides smoothing only of micron-scale speckle, however, which does not affect direct-drive uniformity,[10] and relies on beam overlap within a quad. Polarization smoothing based on glancing angle deposited (GLAD) film is being explored for PDD on the NIF.[72] The proposed polarization smoothing for PDD will be applied to each beam individually to generate two overlapping and noninterfering speckle patterns of orthogonal polarizations per beam.

Finally, modifications to the NIF's Target Handling and Positioning Systems are required to support the fielding of cryogenically cooled, layered direct-drive targets.

Conclusions

Results from a first series of PDD experiments on the NIF have been presented. The campaign is based on polar and symmetric direct-drive experiments performed on the OMEGA laser, which provide a solid foundation for the PDD campaign on the NIF. Room-temperature, 2.2-mm-diam plastic shells were imploded with total drive energies of ~500 to 750 kJ with peak powers of 120 to 180 TW and peak on-target intensities from 8×10^{14} to 1.2×10^{15} W/cm^2. The trajectory and low-mode asymmetry evolution of the imploding shell were measured with x-ray radiography to track the dense shell and with self-emission imaging of the coronal plasma to measure

the ablation surface. Agreement with 2-D *DRACO* simulations was found to improve when the effect of CBET was included in the calculations. These simulations reproduce the radiography data reasonably well, but the ablation surface trajectory is delayed, when compared with simulations, by several hundred picoseconds. Both radiography and self-emission images are reproduced qualitatively by the 2-D *DRACO* simulations, but it is expected that a 3-D treatment is required to fully capture the measured implosion shape.

Evidence of the TPD instability was found by the emission of hard x rays associated with energetic electrons. The hot-electron population for experiments with a nominal intensity of 8×10^{14} W/cm^2 was found to exhibit temperatures of ~45 to 50 keV with a total conversion efficiency of laser energy to hot electrons of ~0.4%. At higher intensities of 1.2×10^{15} W/cm^2, this increased to ~0.8%, while a high-intensity experiment using a Si ablator exhibited only ~0.3% conversion efficiency.

Future dedicated experiments will investigate Rayleigh–Taylor growth from shell surface perturbations and laser imprint in a spherical-implosion PDD platform on the NIF using cone-in-shell targets, CBET mitigation via a hemispheric $\Delta\lambda$ shift, and TPD scaling with plasma scale length and coronal temperature in planar targets.

Additional capabilities and hardware are required to support ignition-scale, cryogenic PDD experiments on the NIF. These capabilities include hemispheric $\Delta\lambda$, improved beam smoothing, dedicated PDD phase plates, and a direct-drive cryogenic target positioner system for direct-drive targets.

REFERENCES

1. J. Nuckolls *et al.*, Nature **239**, 139 (1972).

2. J. D. Lindl, *Inertial Confinement Fusion: The Quest for Ignition and Energy Gain Using Indirect Drive* (Springer-Verlag, New York, 1998).

3. S. Atzeni and J. Meyer-ter-Vehn, *The Physics of Inertial Fusion: Beam Plasma Interaction, Hydrodynamics, Hot Dense Matter, International Series of Monographs on Physics* (Clarendon Press, Oxford, 2004).

4. R. L. McCrory, D. D. Meyerhofer, R. Betti, R. S. Craxton, J. A. Delettrez, D. H. Edgell, V. Yu. Glebov, V. N. Goncharov, D. R. Harding, D. W. Jacobs-Perkins, J. P. Knauer, F. J. Marshall, P. W. McKenty, P. B. Radha, S. P. Regan, T. C. Sangster, W. Seka, R. W. Short, S. Skupsky, V. A. Smalyuk, J. M. Soures, C. Stoeckl, B. Yaakobi, D. Shvarts, J. A. Frenje, C. K. Li, R. D. Petrasso, and F. H. Séguin, Phys. Plasmas **15**, 055503 (2008).

5. S. W. Haan, J. D. Lindl, D. A. Callahan, D. S. Clark, J. D. Salmonson, B. A. Hammel, L. J. Atherton, R. C. Cook, M. J. Edwards, S. Glenzer, A. V. Hamza, S. P. Hatchett, M. C. Herrmann, D. E. Hinkel, D. D. Ho, H. Huang, O. S. Jones, J. Kline, G. Kyrala, O. L. Landen, B. J. MacGowan, M. M. Marinak, D. D. Meyerhofer, J. L. Milovich, K. A. Moreno, E. I. Moses, D. H. Munro, A. Nikroo, R. E. Olson, K. Peterson, S. M. Pollaine, J. E. Ralph, H. F. Robey, B. K. Spears, P. T. Springer, L. J. Suter, C. A. Thomas, R. P. Town, R. Vesey, S. V. Weber, H. L. Wilkens, and D. C. Wilson, Phys. Plasmas **18**, 051001 (2011).

6. G. H. Miller, E. I. Moses, and C. R. Wuest, Opt. Eng. **43**, 2841 (2004).

7. S. W. Haan *et al.*, Phys. Plasmas **2**, 2480 (1995).

8. D. Eimerl, ed., Lawrence Livermore National Laboratory, Livermore, CA, Report UCRL-ID-120758 (1995).

9. S. Skupsky, J. A. Marozas, R. S. Craxton, R. Betti, T. J. B. Collins, J. A. Delettrez, V. N. Goncharov, P. W. McKenty, P. B. Radha, T. R. Boehly, J. P. Knauer, F. J. Marshall, D. R. Harding, J. D. Kilkenny, D. D. Meyerhofer, T. C. Sangster, and R. L. McCrory, Phys. Plasmas **11**, 2763 (2004).

10. T. J. B. Collins, J. A. Marozas, K. S. Anderson, R. Betti, R. S. Craxton, J. A. Delettrez, V. N. Goncharov, D. R. Harding, F. J. Marshall, R. L. McCrory, D. D. Meyerhofer, P. W. McKenty, P. B. Radha, A. Shvydky, S. Skupsky, and J. D. Zuegel, Phys. Plasmas **19**, 056308 (2012).

11. P. B. Radha, F. J. Marshall, J. A. Marozas, A. Shvydky, I. Gabalski, T. R. Boehly, T. J. B. Collins, R. S. Craxton, D. H. Edgell, R. Epstein, J. A. Frenje, D. H. Froula, V. N. Goncharov, M. Hohenberger, R. L. McCrory, P. W. McKenty, D. D. Meyerhofer, R. D. Petrasso, T. C. Sangster, and S. Skupsky, Phys. Plasmas **20**, 056306 (2013).

12. T. R. Boehly, D. L. Brown, R. S. Craxton, R. L. Keck, J. P. Knauer, J. H. Kelly, T. J. Kessler, S. A. Kumpan, S. J. Loucks, S. A. Letzring, F. J. Marshall, R. L. McCrory, S. F. B. Morse, W. Seka, J. M. Soures, and C. P. Verdon, Opt. Commun. **133**, 495 (1997).

13. V. N. Goncharov, T. C. Sangster, T. R. Boehly, S. X. Hu, I. V. Igumenshchev, F. J. Marshall, R. L. McCrory, D. D. Meyerhofer, P. B. Radha, W. Seka, S. Skupsky, C. Stoeckl, D. T. Casey, J. A. Frenje, and R. D. Petrasso, Phys. Rev. Lett. **104**, 165001 (2010).

14. T. C. Sangster, V. N. Goncharov, R. Betti, P. B. Radha, T. R. Boehly, D. T. Casey, T. J. B. Collins, R. S. Craxton, J. A. Delettrez, D. H. Edgell, R. Epstein, C. J. Forrest, J. A. Frenje, D. H. Froula, M. Gatu-Johnson, V. Yu. Glebov, D. R. Harding, M. Hohenberger, S. X. Hu, I. V. Igumenshchev, R. Janezic, J. H. Kelly, T. J. Kessler, C. Kingsley,

T. Z. Kosc, J. P. Knauer, S. J. Loucks, J. A. Marozas, F. J. Marshall, A. V. Maximov, R. L. McCrory, P. W. McKenty, D. D. Meyerhofer, D. T. Michel, J. F. Myatt, R. D. Petrasso, S. P. Regan, W. Seka, W. T. Shmayda, R. W. Short, A. Shvydky, S. Skupsky, J. M. Soures, C. Stoeckl, W. Theobald, V. Versteeg, B. Yaakobi, and J. D. Zuegel, Phys. Plasmas **20**, 056317 (2013).

15. P. J. Wegner *et al.*, in *Optical Engineering at the Lawrence Livermore National Laboratory II: The National Ignition Facility*, edited by M. A. Lane and C. R. Wuest (SPIE, Bellingham, WA, 2004), Vol. 5341, pp. 180–189.

16. B. J. MacGowan *et al.*, Phys. Plasmas **3**, 2029 (1996).

17. C. A. Haynam *et al.*, Appl. Opt. **46**, 3276 (2007).

18. A. M. Cok, R. S. Craxton, and P. W. McKenty, Phys. Plasmas **15**, 082705 (2008).

19. P. B. Radha, V. N. Goncharov, T. J. B. Collins, J. A. Delettrez, Y. Elbaz, V. Yu. Glebov, R. L. Keck, D. E. Keller, J. P. Knauer, J. A. Marozas, F. J. Marshall, P. W. McKenty, D. D. Meyerhofer, S. P. Regan, T. C. Sangster, D. Shvarts, S. Skupsky, Y. Srebro, R. P. J. Town, and C. Stoeckl, Phys. Plasmas **12**, 032702 (2005).

20. C. J. Randall, J. R. Albritton, and J. J. Thomson, Phys. Fluids **24**, 1474 (1981).

21. D. T. Michel, C. Sorce, R. Epstein, N. Whiting, I. V. Igumenshchev, R. Jungquist, and D. H. Froula, Rev. Sci. Instrum. **83**, 10E530 (2012).

22. M. Hohenberger, F. Albert, N. E. Palmer, J. J. Lee, T. Döppner, L. Divol, E. L. Dewald, B. Bachmann, A. G. MacPhee, G. LaCaille, D. K. Bradley, and C. Stoeckl, Rev. Sci. Instrum. **85**, 11D501 (2014).

23. M. N. Rosenbluth, R. B. White, and C. S. Liu, Phys. Rev. Lett. **31**, 1190 (1973).

24. J. F. Myatt, J. Zhang, R. W. Short, A. V. Maximov, W. Seka, D. H. Froula, D. H. Edgell, D. T. Michel, I. V. Igumenshchev, D. E. Hinkel, P. Michel, and J. D. Moody, Phys. Plasmas **21**, 055501 (2014).

25. M. V. Goldman, Ann. Phys. **38**, 117 (1966).

26. P. B. Radha, V. N. Goncharov, M. Hohenberger, T. C. Sangster, R. Betti, R. S. Craxton, D. H. Edgell, R. Epstein, D. H. Froula, J. A. Marozas, F. J. Marshall, R. L. McCrory, P. W. McKenty, D. D. Meyerhofer, D. T. Michel, S. X. Hu, W. Seka, A. Shvydky, S. Skupsky, J. A. Frenje, M. Gatu Johnson, R. D. Petrasso, T. Ma, S. Le Pape, and A. J. Mackinnon, "Direct-Drive Implosion Physics: Results from OMEGA and the National Ignition Facility," to be published in the Journal of Physics: Conference Series.

27. J. A. Marozas, F. J. Marshall, R. S. Craxton, I. V. Igumenshchev, S. Skupsky, M. J. Bonino, T. J. B. Collins, R. Epstein, V. Yu. Glebov, D. Jacobs-Perkins, J. P. Knauer, R. L. McCrory, P. W. McKenty, D. D. Meyerhofer, S. G. Noyes, P. B. Radha, T. C. Sangster, W. Seka, and V. A. Smalyuk, Phys. Plasmas **13**, 056311 (2006).

28. W. F. Huebner *et al.*, Los Alamos National Laboratory, Los Alamos, NM, Report LA-6760-M (1977).

29. N. A. Ebrahim *et al.*, Phys. Rev. Lett. **45**, 1179 (1980).

30. J. F. Myatt, J. Zhang, J. A. Delettrez, A. V. Maximov, R. W. Short, W. Seka, D. H. Edgell, D. F. DuBois, D. A. Russell, and H. X. Vu, Phys. Plasmas **19**, 022707 (2012).

31. B. Yaakobi, P.-Y. Chang, A. A. Solodov, C. Stoeckl, D. H. Edgell, R. S. Craxton, S. X. Hu, J. F. Myatt, F. J. Marshall, W. Seka, and D. H. Froula, Phys. Plasmas **19**, 012704 (2012).

32. J. A. Oertel *et al.*, Rev. Sci. Instrum. **77**, 10E308 (2006).

33. G. A. Kyrala *et al.*, Rev. Sci. Instrum. **81**, 10E316 (2010).

34. J. D. Moody *et al.*, Rev. Sci. Instrum. **81**, 10D921 (2010).

35. V. Yu. Glebov, T. C. Sangster, C. Stoeckl, J. P. Knauer, W. Theobald, K. L. Marshall, M. J. Shoup III, T. Buczek, M. Cruz, T. Duffy, M. Romanofsky, M. Fox, A. Pruyne, M. J. Moran, R. A. Lerche, J. McNaney, J. D. Kilkenny, M. J. Eckart, D. Schneider, D. Munro, W. Stoeffl, R. Zacharias, J. J. Haslam, T. Clancy, M. Yeoman, D. Warwas, C. J. Horsfield, J.-L. Bourgade, O. Landoas, L. Disdier, G. A. Chandler, and R. J. Leeper, Rev. Sci. Instrum. **81**, 10D325 (2010).

36. H. G. Rinderknecht, M. Gatu Johnson, A. B. Zylstra, N. Sinenian, M. J. Rosenberg, J. A. Frenje, C. J. Waugh, C. K. Li, F. H. Séguin, R. D. Petrasso, J. R. Rygg, J. R. Kimbrough, A. MacPhee, G. W. Collins, D. Hicks, A. Mackinnon, P. Bell, R. Bionta, T. Clancy, R. Zacharias, T. Döppner, H. S. Park, S. LePape, O. Landen, N. Meezan, E. I. Moses, V. Yu. Glebov, C. Stoeckl, T. C. Sangster, R. Olson, J. Kline, and J. Kilkenny, Rev. Sci. Instrum. **83**, 10D902 (2012).

37. A. B. Zylstra, J. A. Frenje, F. H. Séguin, M. J. Rosenberg, H. G. Rinderknecht, M. Gatu Johnson, D. T. Casey, N. Sinenian, M. J. E. Manuel, C. J. Waugh, H. W. Sio, C. K. Li, R. D. Petrasso, S. Friedrich, K. Knittel, R. Bionta, M. McKernan, D. Callahan, G. W. Collins, E. Dewald, T. Doppner, M. J. Edwards, S. Glenzer, D. G. Hicks, O. L. Landen, R. London, A. Mackinnon, N. Meezan, R. R. Prasad, J. Ralph, M. Richardson, J. R. Rygg, S. Sepke, S. Weber, R. Zacharias, E. Moses, J. Kilkenny, A. Nikroo, T. C. Sangster, V. Glebov, C. Stoeckl, R. Olson, R. J. Leeper, J. Kline, G. Kyrala, and D. Wilson, Rev. Sci. Instrum. **83**, 10D901 (2012).

38. M. J. Schmitt, P. A. Bradley, J. A. Cobble, J. R. Fincke, P. Hakel, S. C. Hsu, N. S. Krasheninnikova, G. A. Kyrala, G. R. Magelssen, D. S. Montgomery, T. J. Murphy, K. A. Obrey, R. C. Shah, I. L. Tregillis, J. A. Baumgaertel, F. J. Wysocki, S. H. Batha, R. S. Craxton, P. W. McKenty, P. Fitzsimmons, A. Nikroo, and R. Wallace, Phys. Plasmas **20**, 056310 (2013).

39. J. J. MacFarlane *et al.*, High Energy Density Phys. **3**, 181 (2007).

40. S. E. Bodner, Phys. Rev. Lett. **33**, 761 (1974).

41. S. Chandrasekhar, in *Hydrodynamic and Hydromagnetic Stability*, International Series of Monographs on Physics (Clarendon Press, Oxford, 1961).

42. D. H. Froula, I. V. Igumenshchev, D. T. Michel, D. H. Edgell, R. Follett, V. Yu. Glebov, V. N. Goncharov, J. Kwiatkowski, F. J. Marshall, P. B.

Radha, W. Seka, C. Sorce, S. Stagnitto, C. Stoeckl, and T. C. Sangster, Phys. Rev. Lett. **108**, 125003 (2012).

43. D. T. Michel, V. N. Goncharov, I. V. Igumenshchev, R. Epstein, and D. H. Froula, Phys. Rev. Lett. **111**, 245005 (2013).

44. M. M. Marinak *et al.*, Phys. Plasmas **8**, 2275 (2001).

45. P. B. Radha, C. Stoeckl, V. N. Goncharov, J. A. Delettrez, D. H. Edgell, J. A. Frenje, I. V. Igumenshchev, J. P. Knauer, J. A. Marozas, R. L. McCrory, D. D. Meyerhofer, R. D. Petrasso, S. P. Regan, T. C. Sangster, W. Seka, and S. Skupsky, Phys. Plasmas **18**, 012705 (2011).

46. A. Shvydky, M. Hohenberger, P. B. Radha, R. S. Craxton, V. N. Goncharov, J. A. Marozas, F. J. Marshall, P. W. McKenty, and T. C. Sangster, Bull. Am. Phys. Soc. **59**, 330 (2014).

47. D. H. Froula, D. T. Michel, I. V. Igumenshchev, S. X. Hu, B. Yaakobi, J. F. Myatt, D. H. Edgell, R. Follett, V. Yu. Glebov, V. N. Goncharov, T. J. Kessler, A. V. Maximov, P. B. Radha, T. C. Sangster, W. Seka, R. W. Short, A. A. Solodov, C. Sorce, and C. Stoeckl, Plasma Phys. Control. Fusion **54**, 124016 (2012).

48. W. Seka, D. H. Edgell, J. F. Myatt, A. V. Maximov, R. W. Short, V. N. Goncharov, and H. A. Baldis, Phys. Plasmas **16**, 052701 (2009).

49. B. Yaakobi, A. A. Solodov, J. F. Myatt, J. A. Delettrez, C. Stoeckl, and D. H. Froula, Phys. Plasmas **20**, 092706 (2013).

50. D. H. Froula, B. Yaakobi, S. X. Hu, P.-Y. Chang, R. S. Craxton, D. H. Edgell, R. Follett, D. T. Michel, J. F. Myatt, W. Seka, R. W. Short, A. Solodov, and C. Stoeckl, Phys. Rev. Lett. **108**, 165003 (2012).

51. C. Stoeckl, R. E. Bahr, B. Yaakobi, W. Seka, S. P. Regan, R. S. Craxton, J. A. Delettrez, R. W. Short, J. Myatt, A. V. Maximov, and H. Baldis, Phys. Rev. Lett. **90**, 235002 (2003).

52. A. Simon, R. W. Short, E. A. Williams, and T. Dewandre, Phys. Fluids **26**, 3107 (1983).

53. D. T. Michel, A. V. Maximov, R. W. Short, S. X. Hu, J. F. Myatt, W. Seka, A. A. Solodov, B. Yaakobi, and D. H. Froula, Phys. Rev. Lett. **109**, 155007 (2012).

54. J. Zhang, J. F. Myatt, R. W. Short, A. V. Maximov, H. X. Vu, D. F. DuBois, and D. A. Russell, Phys. Rev. Lett. **113**, 105001 (2014).

55. R. W. Short, J. F. Myatt, and J. Zhang, Bull. Am. Phys. Soc. **58**, 27 (2013).

56. K. A. Brueckner, Phys. Rev. Lett. **36**, 677 (1976).

57. R. P. Drake *et al.*, Phys. Rev. A **40**, 3219 (1989).

58. T. Döppner *et al.*, Phys. Rev. Lett. **108**, 135006 (2012).

59. J. A. Delettrez, T. J. B. Collins, and C. Ye, Bull. Am. Phys. Soc. **59**, 150 (2014).

60. V. A. Smalyuk, R. Betti, J. A. Delettrez, V. Yu. Glebov, D. D. Meyerhofer, P. B. Radha, S. P. Regan, T. C. Sangster, J. Sanz, W. Seka, C. Stoeckl, B. Yaakobi, J. A. Frenje, C. K. Li, R. D. Petrasso, and F. H. Séguin, Phys. Rev. Lett. **104**, 165002 (2010).

61. J. F. Myatt, H. X. Vu, D. F. DuBois, D. A. Russell, J. Zhang, R. W. Short, and A. V. Maximov, Phys. Plasmas **20**, 052705 (2013).

62. D. T. Michel, A. V. Maximov, R. W. Short, J. A. Delettrez, D. Edgell, S. X. Hu, I. V. Igumenshchev, J. F. Myatt, A. A. Solodov, C. Stoeckl, B. Yaakobi, and D. H. Froula, Phys. Plasmas **20**, 055703 (2013).

63. V. N. Goncharov, T. C. Sangster, R. Betti, T. R. Boehly, M. J. Bonino, T. J. B. Collins, R. S. Craxton, J. A. Delettrez, D. H. Edgell, R. Epstein, R. K. Follet, C. J. Forrest, D. H. Froula, V. Yu. Glebov, D. R. Harding, R. J. Henchen, S. X. Hu, I. V. Igumenshchev, R. Janezic, J. H. Kelly, T. J. Kessler, T. Z. Kosc, S. J. Loucks, J. A. Marozas, F. J. Marshall, A. V. Maximov, R. L. McCrory, P. W. McKenty, D. D. Meyerhofer, D. T. Michel, J. F. Myatt, R. Nora, P. B. Radha, S. P. Regan, W. Seka, W. T. Shmayda, R. W. Short, A. Shvydky, S. Skupsky, C. Stoeckl, B. Yaakobi, J. A. Frenje, M. Gatu Johnson, R. D. Petrasso, and D. T. Casey, Phys. Plasmas **21**, 056315 (2014).

64. V. A. Smalyuk, M. Barrios, J. A. Caggiano, D. T. Casey, C. J. Cerjan, D. S. Clark, M. J. Edwards, J. A. Frenje, M. Gatu-Johnson, V. Yu. Glebov, G. Grim, S. W. Haan, B. A. Hammel, A. Hamza, D. E. Hoover, W. W. Hsing, O. Hurricane, J. D. Kilkenny, J. L. Kline, J. P. Knauer, J. Kroll, O. L. Landen, J. D. Lindl, T. Ma, J. M. McNaney, M. Mintz, A. Moore, A. Nikroo, T. Parham, J. L. Peterson, R. Petrasso, L. Pickworth, J. E. Pino, K. Raman, S. P. Regan, B. A. Remington, H. F. Robey, D. P. Rowley, D. B. Sayre, R. E. Tipton, S. V. Weber, K. Widmann, D. C. Wilson, and C. B. Yeamans, Phys. Plasmas **21**, 056301 (2014).

65. G. Fiksel, S. X. Hu, V. N. Goncharov, D. D. Meyerhofer, T. C. Sangster, V. A. Smalyuk, B. Yaakobi, M. J. Bonino, and R. Jungquist, Phys. Plasmas **19**, 062704 (2012).

66. I. V. Igumenshchev, W. Seka, D. H. Edgell, D. T. Michel, D. H. Froula, V. N. Goncharov, R. S. Craxton, L. Divol, R. Epstein, R. Follett, J. H. Kelly, T. Z. Kosc, A. V. Maximov, R. L. McCrory, D. D. Meyerhofer, P. Michel, J. F. Myatt, T. C. Sangster, A. Shvydky, S. Skupsky, and C. Stoeckl, Phys. Plasmas **19**, 056314 (2012).

67. J. A. Marozas, T. J. B. Collins, P. W. McKenty, J. D. Zuegel, P. B. Radha, F. J. Marshall, W. Seka, D. T. Michel, and M. Hohenberger, Bull. Am. Phys. Soc. **59**, 201 (2014).

68. J. A. Marozas, T. J. B. Collins, J. D. Zuegel, P. B. Radha, F. J. Marshall, and W. Seka, "Cross-Beam Energy Transfer Mitigation Strategy for NIF Polar Drive," presented at the 44th Annual Anomalous Absorption Conference, Estes Park, CO, 8–13 June 2014.

69. J. A. Marozas, J. D. Zuegel, and T. J. B. Collins, Bull. Am. Phys. Soc. **55**, 294 (2010).

70. T. R. Boehly, V. A. Smalyuk, D. D. Meyerhofer, J. P. Knauer, D. K. Bradley, R. S. Craxton, M. J. Guardalben, S. Skupsky, and T. J. Kessler, J. Appl. Phys. **85**, 3444 (1999).

71. S. P. Regan, J. A. Marozas, R. S. Craxton, J. H. Kelly, W. R. Donaldson, P. A. Jaanimagi, D. Jacobs-Perkins, R. L. Keck, T. J. Kessler, D. D. Meyerhofer, T. C. Sangster, W. Seka, V. A. Smalyuk, S. Skupsky, and J. D. Zuegel, J. Opt. Soc. Am. B **22**, 998 (2005).

72. J. B. Oliver, T. J. Kessler, C. Smith, B. Taylor, V. Gruschow, J. Hettrick, and B. Charles, Opt. Express **22**, 23883 (2014).